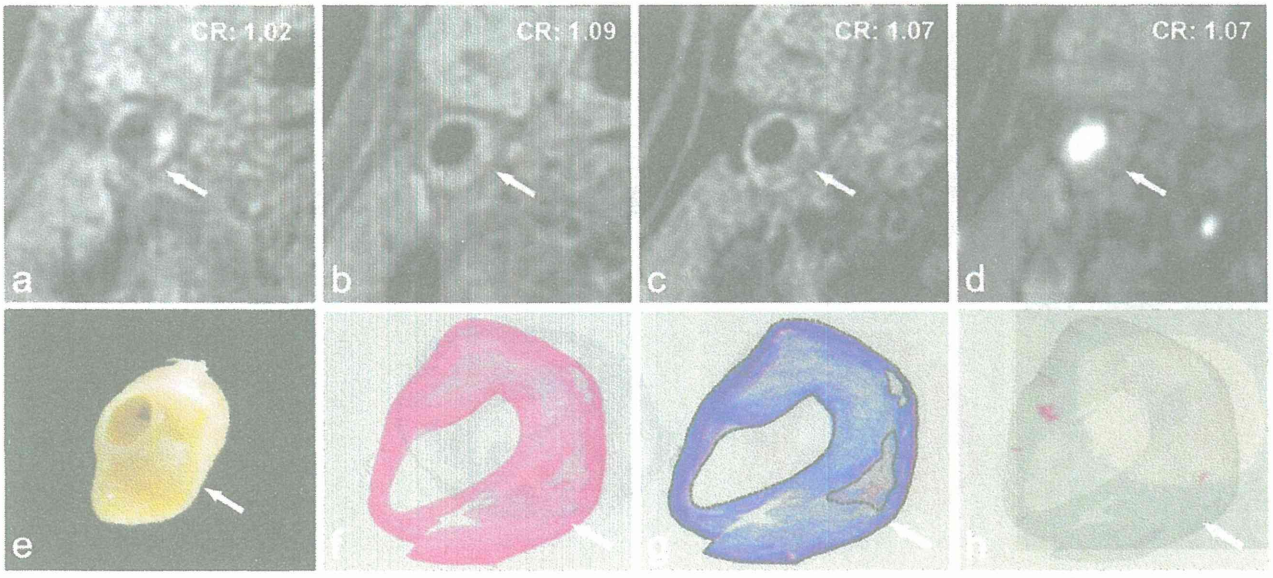

Fig. 2 T1-weighted MR images obtained by different techniques and corresponding pathological findings of the carotid plaque containing mainly fibrous tissue (75-year-old man with right carotid stenosis). **a** Non-gated SE; **b** BB-FSE; **c** MPRAGE; **d** SI-MRA; **e** macroscopic specimen; **f**, **g**, **h** histological specimens with hematoxylin–eosin, Masson-trichrome, and antiglycophorin-A staining methods, respectively. *CR* contrast ratio. On all MR images, the plaque shows near isointensity to the adjacent muscle (a–d, arrows). On macroscopic and microscopic specimens, the plaque consists mainly of fibrous tissue (delineated by *dotted lines*, 90% of the entire plaque area) (e–g, *arrows*)

was less conspicuous than that of the other methods. Using BB-FSE, TR is forced to depend on a one R–R interval, resulting in a TR of 800–1,000 ms, which is too long to diminish proton-density weighted contrast and to enhance T1W contrast [11]. Thus, inappropriately long TR can deteriorate the contrast originating from lipid and hemorrhagic

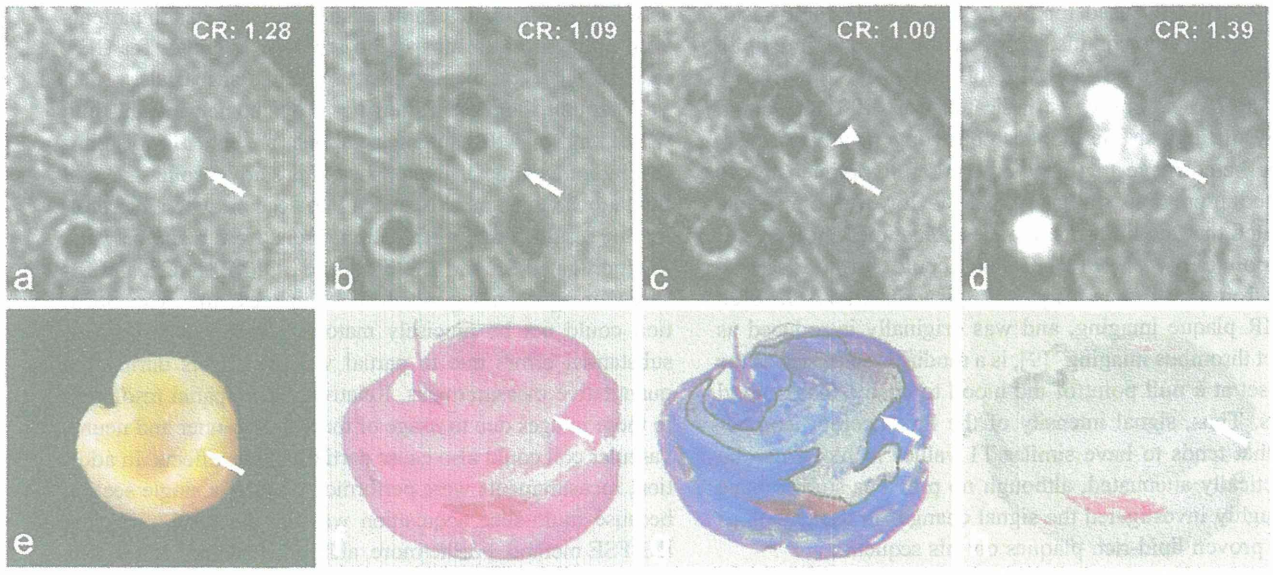

Fig. 3 T1-weighted MR images obtained by different techniques and corresponding pathological findings of the carotid plaque containing mainly lipid and necrosis (71-year-old man with left carotid stenosis). **a** Non-gated SE; **b** BB-FSE; **c** MPRAGE; **d** SI-MRA; **e** macroscopic specimen; **f**, **g**, **h** histological specimens with hematoxylin–eosin, Masson-trichrome, and antiglycophorin-A staining methods, respectively. *CR* contrast ratio. The plaque shows moderate hyperintensity on non-gated SE and SI-MRA images, but almost isointensity on BB-FSE and MP-RAGE (**a**–**d**, *arrows*). In addition, a part of the plaque shows hypointensity on MPRAGE (c, *arrowhead*). Pathological specimens show that the plaque consists of lipid/necrotic component (delineated by *dotted lines*, 52% of the entire plaque area) (e–h, *arrows*)

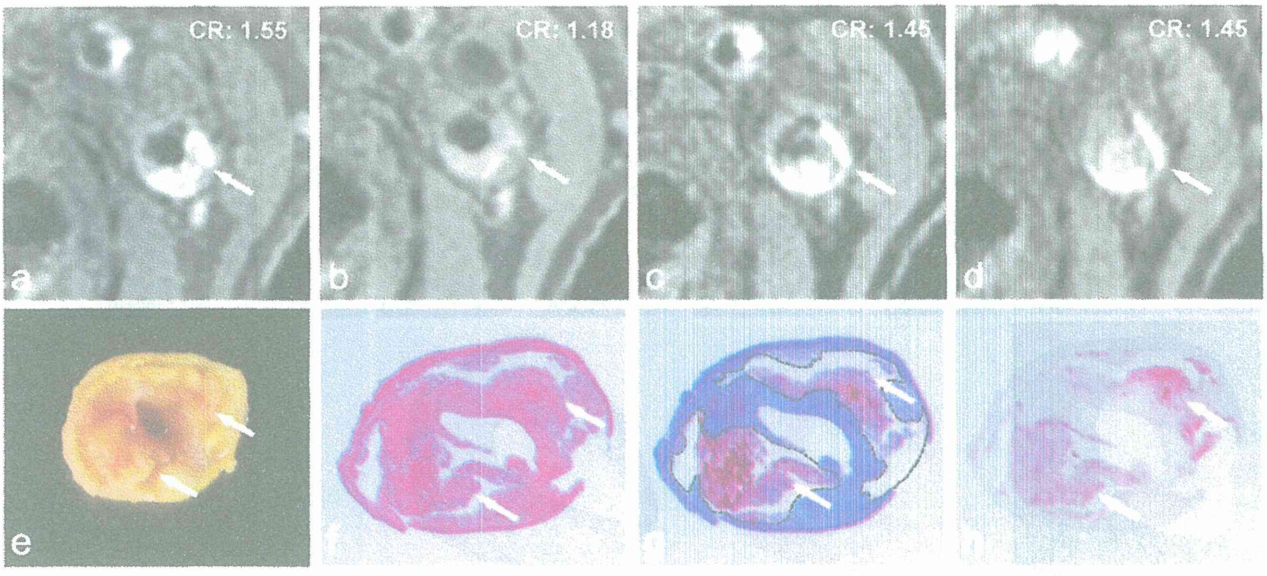

Fig. 4 T1-weighted MR images obtained by different techniques and corresponding pathological findings of the carotid plaque containing mainly hemorrhage (73-year-old man with left carotid stenosis). **a** Non-gated SE, **b** BB-FSE, **c** MPRAGE, **d** SI-MRA, **e** macroscopic specimen; **f**, **g**, **h** histological specimens with hematoxylin–eosin, Masson-trichrome, and antiglycophorin-A staining methods, respectively. *CR* contrast ratio. The plaque shows evident hyperintensity on non-gated SE, MPRAGE, and SI-MRA images (**a**, **c**, **d**; *arrows*), but mild hyperintensity on BB-FSE (**b**, *arrow*). A low signal spot at the anterior margin of the plaque may indicate small calcification. Pathological specimens show that the plaque contains massive hemorrhage (delineated by *dotted lines*, 53% of the entire plaque area) (**e**–**g**, *arrows*)

components within the plaques, which appears to be an inherent disadvantage of this technique. Besides the cardiac gating, proton-density weighted contrast is known to be substantially preserved on T1W spoiled GRE techniques that are generally used for MRA; this feature could result in an insufficient contrast between the fibrous and lipid/necrotic plaques on SI-MRA in this study.

In the present study, we indicated that MPRAGE could readily distinguish the plaques consisting mainly of intraplaque hemorrhage that showed marked hyperintensity, as reported in previous studies [4, 9, 15]. However, our results indicated that the lipid-rich plaques sometimes showed iso- or hypointensity on MPRAGE and could not be discriminated from the fibrous plaques. In general, MPRAGE used for MR plaque imaging, and was originally introduced as "direct thrombus imaging" [9], is a modified sequence as the TI is set at a null point of the blood to enable black-blood effects. Thus, signal intensity of the lipid/necrotic component that tends to have similar T1 values to blood can be theoretically attenuated, although no previous studies have thoroughly investigated the signal changes in the pathologically proven lipid-rich plaques on this sequence.

We showed that non-gated SE, which is a classical standard sequence, showed excellent intraplaque contrast and could discriminate plaques with different components better than BB-FSE, MPRAGE, and SI-MRA. These results can be explained by the fact that this can avoid substantial influences of the proton density and inversion recovery pulse. Non-gated SE needs a relatively long acquisition time, and is relatively susceptible to patient motions even when using a motion correction technique; however, this method is widely applicable in any scanners, can be used for assessing intraplaque characteristics and changes in patients with mild carotid stenosis who are not candidates for CEA or CAS [16], and may be used for multicenter trials.

Although, the present study has provided new insights into which kinds of MR imaging techniques are better for discriminating intraplaque characteristics, this study also has several limitations which must be taken into account when interpreting the results. First, direct comparisons were made between 2D (non-gated SE and BB-FSE) and 3D (MPRAGE and SI-MRA) images, among which slice thickness and image location could not be precisely matched. This could result in substantial errors due to partial volume effects during the quantitative measurements. Relatively low spatial resolution in these images due to usage of the 1.5-T scanner and neurovascular coil could also cause partial volume effects. In addition, measurements were performed on only a single section because multi-slice acquisition was not available using the BB-FSE method. Furthermore, although histological sections were carefully prepared, locations of MR images were not matched perfectly to those of the histology specimens. These issues may decrease the reliability and reproducibility of the results in this study to some extent.

Another limitation of this study is that signal intensity of the entire plaque was measured by a manual tracing

technique to calculate the CR. Intraplaque components are usually heterogeneous so that CRs in this study reflect a mixture of fibrous, lipid/necrotic, and hemorrhagic components with various percentages. Presence of calcification, which was occasionally observed in the plaques, also can affect the CR values; we did not assess this in this study because T1W images we used poorly visualize the calcific component. Further, plaques containing massive hemorrhagic or lipid/necrotic components with a thin fibrous cap can be unstable, even if the principal component is fibrous tissue and/or calcification. Manual tracing also can affect reproducibility of the measurements among the different images and sessions. For more precise comparisons among MR images and histopathological images, including assessment of the thickness of the fibrous cap, sub-regional measurements or measurements on a pixel-by-pixel basis are required.

In addition, this study could not accurately determine sensitivity and specificity of the four kinds of imaging techniques for discriminating plaques that consist mainly of lipid/necrosis and/or hemorrhage from plaques that consist mainly of fibrous tissue. This is due to the relatively small number of patients involved in the study, which included only five cases of fibrous plaques. Further investigation with a larger sample size is necessary to confirm our results. This study also did not clarify whether novel 3D-FSE techniques [17, 18] have sufficient contrast as compared with the classical techniques, whether addition of other images, such as T2-weighted images, can contribute to further discrimination of the intraplaque components [19], whether visual interpretation can accurately characterize the plaques as compared with signal measurements, or whether differences in the static magnetic field affect intraplaque contrast because there are substantial differences in signal-to-noise, spatial resolution, T1 relaxation, and susceptibility effects between 1.5 and 3 T [20]. These parameters, although beyond the scope of this manuscript, should also be investigated further.

In conclusion, contrast of T1W MR plaque imaging significantly varied among the four kinds of imaging techniques examined here. Importantly, images obtained using non-gated SE method can more accurately characterize main intraplaque components in patients who underwent CEA when compared with other imaging techniques, such as cardiac-gated BB-FSE, MPRAGE, and SI-MRA methods.

Acknowledgements This work was supported in part by a Research Grant for Cardiovascular Diseases (20C-1) from the Ministry of Heath, Labor and Welfare of Japan, a Grant-in-Aid for Strategic Medical Science Research Center, and Grants-in-Aid for Science Research (22890169, 22590963) from the Ministry of Education, Culture, Sports, Science and Technology of Japan.

Conflict of interest MS consults for Hitachi Medical Corporation and has received honoraria for lectures from the same company.

References

1. Brott TG, Hobson RW 2nd, Howard G, Roubin GS, Clark WM, Brooks W, Mackey A, Hill MD, Leimgruber PP, Sheffet AJ, Howard VJ, Moore WS, Voeks JH, Hopkins LN, Cutlip DE, Cohen DJ, Popma JJ, Ferguson RD, Cohen SN, Blackshear JL, Silver FL, Mohr JP, Lal BK, Meschia JF (2010) Stenting versus endarterectomy for treatment of carotid-artery stenosis. N Engl J Med 363:11–23
2. Yamada K, Yoshimura S, Kawasaki M, Enomoto Y, Asano T, Hara A, Minatoguchi S, Iwama T (2011) Embolic complications after carotid artery stenting or carotid endarterectomy are associated with tissue characteristics of carotid plaques evaluated by magnetic resonance imaging. Atherosclerosis 215:399–404
3. Takaya N, Yuan C, Chu B, Saam T, Underhill H, Cai J, Tran N, Polissar NL, Isaac C, Ferguson MS, Garden GA, Cramer SC, Maravilla KR, Hashimoto B, Hatsukami TS (2006) Association between carotid plaque characteristics and subsequent ischemic cerebrovascular events: a prospective assessment with MRI—initial results. Stroke 37:818–823
4. Yamada N, Higashi M, Otsubo R, Sakuma T, Oyama N, Tanaka R, Iihara K, Naritomi H, Minematsu K, Naito H (2007) Association between signal hyperintensity on T1-weighted MR imaging of carotid plaques and ipsilateral ischemic events. AJNR Am J Neuroradiol 28:287–292
5. Hatsukami TS, Yuan C (2010) MRI in the early identification and classification of high-risk atherosclerotic carotid plaques. Imaging Med 2:63–75
6. Yoshida K, Narumi O, Chin M, Inoue K, Tabuchi T, Oda K, Nagayama M, Egawa N, Hojo M, Goto Y, Watanabe Y, Yamagata S (2008) Characterization of carotid atherosclerosis and detection of soft plaque with use of black-blood MR imaging. AJNR Am J Neuroradiol 29:868–874
7. Yoshimura S, Yamada K, Kawasaki M, Asano T, Kanematsu M, Takamatsu M, Hara A (2011) High-intensity signal on time-of-flight magnetic resonance angiography indicates carotid plaques at high risk for cerebral embolism during stenting. Stroke 42:3132–3137
8. Watanabe Y, Nagayama M, Suga T, Yoshida K, Yamagata S, Okumura A, Amoh Y, Nakashita S, Van Cauteren M, Dodo Y (2008) Characterization of atherosclerotic plaque of carotid arteries with histopathological correlation: vascular wall MR imaging vs. color Doppler ultrasonography (US). J Magn Reson Imaging 28:478–485
9. Moody AR, Murphy RE, Morgan PS, Martel AL, Delay GS, Allder S, MacSweeney ST, Tennant WG, Gladman J, Lowe J, Hunt BJ (2003) Characterization of complicated carotid plaque with magnetic resonance direct thrombus imaging in patients with cerebral ischemia. Circulation 107:3047–3052
10. Tamhane AA, Arfanakis K (2009) Motion correction in periodically-rotated overlapping parallel lines with enhanced reconstruction (PROPELLER) and turboprop MRI. Magn Reson Med 62:174–182
11. Narumi S, Sasaki M, Ohba H, Ogasawara K, Hitomi J, Mori K, Ohura K, Ono A, Terayama Y (2010) Altered carotid plaque signal among different repetition times on T1-weighted magnetic resonance plaque imaging with self-navigated radial-scan technique. Neuroradiology 52:285–290
12. Yuan C, Mitsumori LM, Beach KW, Maravilla KR (2001) Carotid atherosclerotic plaque: noninvasive MR characterization and identification of vulnerable lesions. Radiology 221:285–299

13. Chu B, Kampschulte A, Ferguson MS, Kerwin WS, Yarnykh VL, O'Brien KD, Polissar NL, Hatsukami TS, Yuan C (2004) Hemorrhage in the atherosclerotic carotid plaque: a high-resolution MRI study. Stroke 35:1079–1084
14. Ota H, Yarnykh VL, Ferguson MS, Underhill HR, Demarco JK, Zhu DC, Oikawa M, Dong L, Zhao X, Collar A, Hatsukami TS, Yuan C (2010) Carotid intraplaque hemorrhage imaging at 3.0-T MR imaging: comparison of the diagnostic performance of three T1-weighted sequences. Radiology 254:551–563
15. Hishikawa T, Iihara K, Yamada N, Ishibashi-Ueda H, Miyamoto S (2010) Assessment of necrotic core with intraplaque hemorrhage in atherosclerotic carotid artery plaque by MR imaging with 3D gradient–echo sequence in patients with high-grade stenosis. Clinical article. J Neurosurg 113:890–896
16. Yamaguchi M, Sasaki M, Ohba H, Mori K, Narumi S, Katsura N, Ohura K, Kudo K, Terayama Y (2012) Quantitative assessment of changes in carotid plaques during cilostazol administration using three-dimensional ultrasonography and non-gated magnetic resonance plaque imaging. Neuroradiology [Epub ahead of print]
17. Balu N, Chu B, Hatsukami TS, Yuan C, Yarnykh VL (2008) Comparison between 2D and 3D high-resolution black-blood techniques for carotid artery wall imaging in clinically significant atherosclerosis. J Magn Reson Imaging 27:918–924
18. Crowe LA, Gatehouse P, Yang GZ, Mohiaddin RH, Varghese A, Charrier C, Keegan J, Firmin DN (2003) Volume-selective 3D turbo spin echo imaging for vascular wall imaging and distensibility measurement. J Magn Reson Imaging 17:572–580
19. Cappendijk VC, Heeneman S, Kessels AG, Cleutjens KB, Schurink GW, Welten RJ, Mess WH, van Suylen RJ, Leiner T, Daemen MJ, van Engelshoven JM, Kooi ME (2008) Comparison of single-sequence T1w TFE MRI with multisequence MRI for the quantification of lipid-rich necrotic core in atherosclerotic plaque. J Magn Reson Imaging 27:1347–1355
20. Underhill HR, Yarnykh VL, Hatsukami TS, Wang J, Balu N, Hayes CE, Oikawa M, Yu W, Xu D, Chu B, Wyman BT, Polissar NL, Yuan C (2008) Carotid plaque morphology and composition: initial comparison between 1.5- and 3.0-T magnetic field strengths. Radiology 248:550–560

THE JOURNAL OF BIOLOGICAL CHEMISTRY VOL. 287, NO. 5, pp. 3349–3356, January 27, 2012

Caldesmon Regulates Axon Extension through Interaction with Myosin II*

Received for publication, August 18, 2011, and in revised form, November 27, 2011 Published, JBC Papers in Press, December 9, 2011, DOI 10.1074/jbc.M111.295618

Tsuyoshi Morita[‡], **Taira Mayanagi**[‡§], **and Kenji Sobue**[‡§1]

From the [‡]*Department of Neuroscience, Osaka University Graduate School of Medicine, 2-2 Yamadaoka, Suita, Osaka 565-0871, Japan and the* [§]*Department of Neuroscience, Institute for Biomedical Sciences, Iwate Medical University, 2-1-1 Nishitokuta, Yahaba-cho, Shiwa-gun, Iwate 028-3694, Japan*

Background: Axon extension, an essential step for creating neural circuits, is regulated by cytoskeletal dynamics.
Results: Caldesmon is a regulator of the actin cytoskeleton and enhances axon extension through direct interaction with myosin II.
Conclusion: Caldesmon binding to myosin II inhibits myosin II function, resulting in the enhancement of axon extension.
Significance: This study elucidates how caldesmon-regulated actin-myosin system is involved in axon extension.

To begin the process of forming neural circuits, new neurons first establish their polarity and extend their axon. Axon extension is guided and regulated by highly coordinated cytoskeletal dynamics. Here we demonstrate that in hippocampal neurons, the actin-binding protein caldesmon accumulates in distal axons, and its N-terminal interaction with myosin II enhances axon extension. In cortical neural progenitor cells, caldesmon knockdown suppresses axon extension and neuronal polarity. These results indicate that caldesmon is an important regulator of axon development.

Neurons in the developing brain extend axonal and dendritic arbors that create a complex circuitry, and the guided extension of axonal fibers is an essential step in this process. Axon extension is regulated by the coordinated interaction of microtubules and actin filaments in the axonal growth cone. A growing body of evidence indicates that microtubule polymerization and stabilization play positive roles in axon extension (1), whereas actin filament roles are more complicated. For example, knocking out Ena/VASP or Cdc42, which positively regulate actin polymerization, causes axonal tract loss (2, 3). In contrast, inhibiting the actin nucleation factor Arp2/3 and pharmacologically destabilizing actin filaments enhances axon extension (4, 5). Thus, the fundamental details of axon guidance and regulation by actin filaments are not well understood.

Caldesmon (CaD)[2] was first identified as a smooth-muscle protein that binds calmodulin and actin (6). It has since been found to be ubiquitously expressed in smooth muscle and non-muscle cells, and to regulate Ca^{2+}-dependent actomyosin contraction (7, 8). CaD binds to the side of filamentous actin (F-actin) and inhibits actin-myosin interactions, as revealed by superprecipitation assays and actin-activated myosin ATPase activity (9–11). CaD binding also stabilizes F-actin filaments by enhancing actin-tropomyosin binding and preventing the actin-severing activity of gelsolin or cofilin (12, 13). CaD plays important roles in migration of non-muscle cells via regulating actin-myosin system (8). We recently reported that CaD is involved in detrimental glucocorticoid-induced effects during cortical brain development (14, 15): glucocorticoids increase CaD levels, transiently retarding the radial migration of cortical neuronal progenitor cells. We also reported that CaD localizes to neuronal growth cones (16). Thus, it seems that CaD plays multiple important roles in neuronal development. In this report, we demonstrate a novel role for CaD in axon extension via its N-terminal myosin binding sequence.

EXPERIMENTAL PROCEDURES

Materials—The myosin II ATPase inhibitor blebbistatin, the myosin light chain kinase inhibitor ML-7, and the Rho-associated protein kinase inhibitor Y27632 were purchased from Merck. The following antibodies were purchased: anti-tau1 (Chemicon), anti-MAP2 (Chemicon), anti-nonmuscle myosin IIA (Abcam), anti-nonmuscle myosin IIB (Abcam), anti-GFP (Invitrogen), anti-FLAG (Sigma), anti-Myc (9E10, Santa Cruz Biotechnology), and anti-GAPDH (FL-335, Santa Cruz Biotechnology). Anti-CaD antibody was generated as previously described (17).

Cell Culture and Immunostaining—Hippocampal neurons were prepared from rat hippocampi on embryonic day 18.5. The dissociated neurons were plated on poly-L-lysine-coated coverslips, and cultured in glial-conditioned MEM containing 1 mM pyruvate, 0.6% (w/v) D-glucose, and 2% B27 supplement (Invitrogen). The next day, the culture was changed to a neurobasal medium containing 2% B27 supplement and 0.5 mM L-glutamine. Cortical NPCs were prepared from rat cerebral cortex on embryonic day 15.5 (E15.5), cultured as previously described (14), plated on laminin-coated coverslips, and cultured under basic FGF-free conditions to induce their differentiation into polarized neurons. A549 and HEK293T cells were cultured in Dulbecco's modified Eagle's medium supplemented with 10% fetal calf serum. Cells cultured on coverslips were fixed using 4% paraformaldehyde and then processed for immunocyto-

* This work was supported by Grants-in-aid for Scientific Research 20240038 from the Japan Society for the Promotion of Science (to K. S.) and 23110510 from the Ministry of Education, Culture, Sports, Science and Technology (MEXT) (to K. S.).

[1] To whom correspondence should be addressed: Dept. of Neuroscience, Institute for Biomedical Sciences, Iwate Medical University, 2-1-1 Nishitokuta, Yahaba-cho, Shiwa-gun, Iwate 028-3694, Japan. Tel.: 81-19-651-5710; Fax: 81-19-908-8020; E-mail: ksobue@iwate-med.ac.jp.

[2] The abbreviations used are: CaD, caldesmon; DIV, day *in vitro*; NPCs, neural progenitor cells; FGF, fibroblast growth factor; HMM, heavy meromyosin.

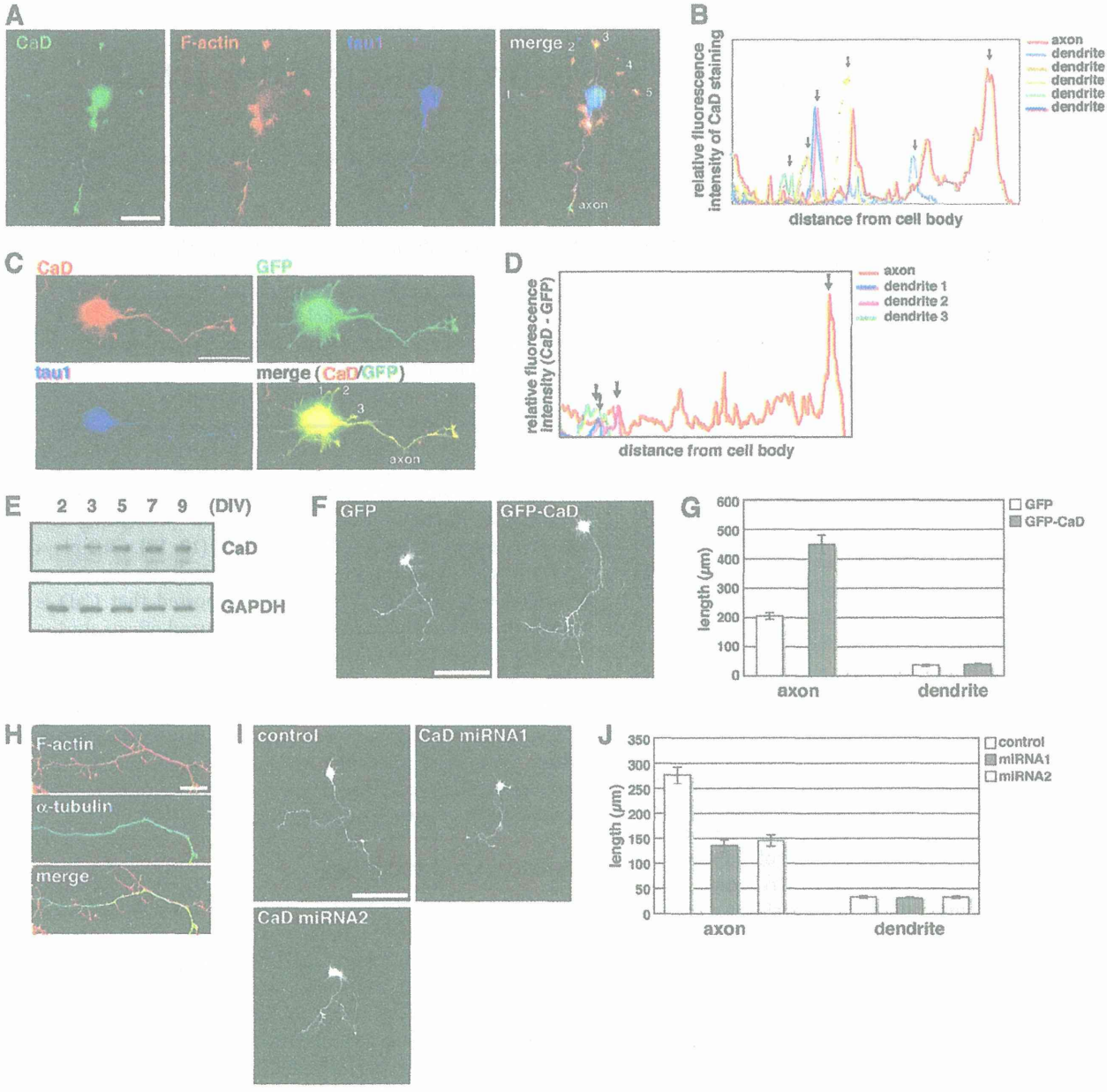

FIGURE 1. **CaD involvement in axon extension.** *A*, CaD protein localization in primary cultured hippocampal neurons. The neurons were fixed and triple-stained with anti-CaD, anti-tau1 antibodies, and phalloidin (F-actin). Bar, 50 μm. *B*, dendrite and axon fluorescence intensities measured in the CaD-immunostained image shown in *A*; *arrows* indicate growth cones. *C*, neurons, which had been transfected with GFP as a cell volume maker, were fixed and triple-stained with anti-CaD, anti-GFP, and anti-tau1 antibodies. Bar, 50 μm. *D*, dendrite and axon fluorescence intensities were measured in the CaD-immunostained and GFP-immunostained images shown in *C*, respectively, and then GFP-intensity was subtracted from CaD-intensity to correct for the influence of cell volume. *Arrows* indicate growth cones. *E*, changes in CaD protein expression during neuronal development. *F*, morphology of GFP- or GFP-CaD-transfected neurons after 3 days in culture (bar, 100 μm) and *G*, quantification of their axonal and dendritic length. Axonal length represents the longest axon branch. Data are means ± S.E. from six independent experiments. *H*, morophlogy of CaD-induced filopodia-like protrusions. The myc-CaD-transfected neurons were fixed and stained with anti-tubulin and phalloidin (F-actin). Bar, 25 μm. *I*, morphology of neurons transfected with control miRNA, CaD miRNA1, or CaD miRNA2, and cultured for 5 days (bar, 100 μm), and *J*, quantification their axonal and dendritic lengths. Data are means ± S.E. from four to six independent experiments.

chemistry. To label F-actin, Alexa 568-phalloidin (Molecular Probes) was added to the secondary antibody solution.

Transfection—Hippocampal neurons prepared from rat embryos on E18.5 were transfected by the calcium phosphate method as described previously (18). In brief, DNA-calcium phosphate precipitates were prepared using a calcium phosphate transfection kit (Invitrogen). The hippocampal neurons were plated on a Nunclon Δ surface plate (Nalge Nunc International) and incubated with the precipitates for 3 h. The transfected neurons were replated on poly-L-lysine-coated coverslips and cultured for 3 to 5 days. A549 and HEK293T cells were transfected using Lipofectamine 2000 or Lipofectamine LTX (Invitrogen).

Expression Plasmids—The coding regions for human l-CaD, its N terminus (1–263 amino acids), C terminus (264–558 amino acids), and N terminus Δ21–47 (lacking amino acids

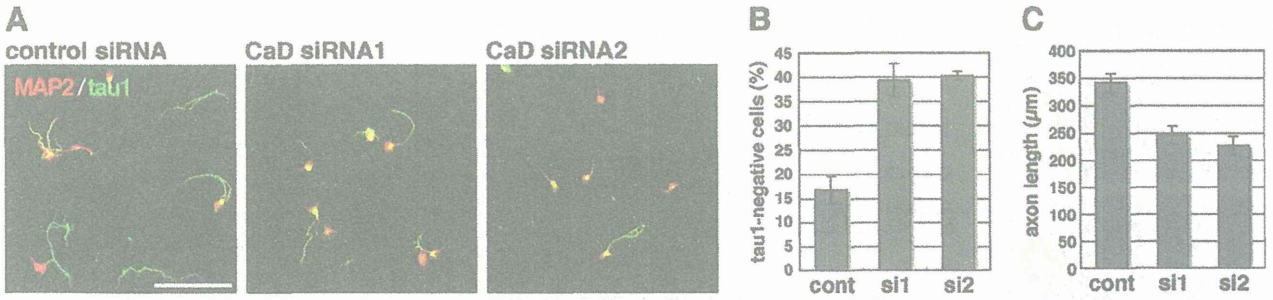

FIGURE 2. **CaD involvement in cortical NPC axon development.** *A*, proliferating cortical NPCs were incubated with control siRNA, CaD siRNA1, or CaD siRNA2 for 3 days, and cultured in basic FGF-free medium for 3 days. The cultured cells were fixed and stained with anti-tau1 (*green*) and anti-MAP2 (*red*) antibodies. Bar, 200 μm. *B*, percentage of tau1-negative non-polarized cells among the differentiating progenitor cells. Data are means ± S.E. from at least 120 cells. *C*, quantification of axonal length in tau1-positive cells. Data are means ± S.E. from at least 30 cells.

21–47 from the N terminus), and the N-terminal fragments of rat myosin IIA (1–1961 amino acids) and IIB (1–1976 amino acids) were amplified by PCR and subcloned into the highly efficient mammalian expression plasmid pCAGGS. EGFP and Myc tag sequences were fused to the 5′-end of the coding sequences. The mcherry-LifeAct expression vector was constructed as previously reported (19).

RNA Interference—Short-interfering RNAs (siRNAs) against rat CaD were transfected into growing cortical NPCs using Lipofectamine RNAi MAX (Invitrogen). MicroRNA (miRNA) plasmids against rat CaD were constructed as previously described (14) and transfected into hippocampal neurons by calcium phosphate precipitation. The targeting sequences and the siRNA and miRNA knockdown efficacy were reported in our previous studies (14, 20).

Immunoprecipitation—HEK293T cells with transfected expression vectors were lysed with Triton-X-buffer (0.05% Triton X-100 (pH 7.6), 30 mM Tris-HCl, 50 mM NaCl 5 mM EGTA, 5 mM $MgCl_2$, 1 mM ATP, and protease inhibitor mixture for use with mammalian cell and tissue extracts (Nacalai Tesque)). Immunoprecipitation was performed using the earlier-listed antibodies and protein G-Sepharose (GE Healthcare Life Sciences). The Sepharose beads were boiled in SDS-sample buffer to elute the immunocomplexes.

RESULTS

CaD Enhances Axon Extension in Hippocampal Neurons—CaD, a ubiquitous regulator of the actin cytoskeleton, localizes along actin fibers and in the ruffling membrane (7, 8). Here, we found that CaD was located in the soma and growth cones of primary cultured hippocampal neurons, with the strongest expression in the distal axon (Fig. 1, *A–D*). CaD levels increased for 3 to 7 days *in vitro* (DIV) (2.3 ± 0.8-fold at 7 DIV *versus* 2 DIV) while the neurons established polarity and actively extended axons (Fig. 1*E*). The location and time-course of CaD expression in these cells are consistent with its having a role in axon extension.

We therefore investigated CaD function in neurite outgrowth by overexpressing or knocking down CaD in hippocampal neurons. We used GFP-fused CaD (GFP-CaD), which has the same functions as endogenous CaD (14, 20). GFP-CaD dramatically enhanced axon extension but did not significantly affect dendrite length as compared with the control, GFP (Fig. 1, *F* and *G*). GFP-CaD also enhanced formation of filopodia-like protrusions from the soma and axon branches (Fig. 1*F*). These CaD-induced protrusions were composed of concentrated actin filaments and were distinct from the main axonal branches, which were filled with microtubules (Fig. 1*H*). Knocking down the endogenous CaD decreased axon length, but not dendritic length (Fig. 1, *I* and *J*), indicating that CaD accumulates in the distal axon of hippocampal neurons during their development and enhances axon extension.

CaD Regulates Axon Development in Cortical NPCs—To monitor CaD involvement in early events in neurite outgrowth, we used cortical neural progenitor cells (NPCs), which proliferate as non-polarized cells in the presence of basic fibroblast growth factor (FGF) (14, 21). Under basic FGF-free conditions, however, NPCs stop proliferating and establish neuronal polarity with MAP2-positive dendrites and a tau1-positive axon (Fig. 2*A*). When CaD was knocked down with siRNAs in proliferating NPCs, tau1-staining showed that the establishment of neuronal polarity was significantly suppressed within three culture days under basic FGF-free conditions (Fig. 2, *A* and *B*). Even in polarized cells, the length of tau1-positive axons was significantly shortened by CaD knockdown (Fig. 2, *A* and *C*), as observed in hippocampal neurons. At an early stage of NPCs differentiation into polarized cells, immature axons were often stained with both anti-MAP2 and anti-tau1 antibodies. In the CaD-knockdown NPCs, some short axons were MAP2/tau1 double positive, suggesting delayed development of these cells. These findings indicate that CaD plays important roles in establishing neuronal polarity and in axon extension in developing NPCs.

CaD-Myosin Interaction Required for Axon Extension—CaD has been reported to bind smooth muscle myosin at its N terminus and F-actin at its C terminus, suggesting that it functions to link these molecules (22). In the growth cone of hippocampal neuronal axons, CaD colocalized with F-actin and myosin IIA/IIB, the major non-muscle isoforms of myosin II (Fig. 3*A*). To examine myosin and actin involvement in CaD-induced axon extension, CaD N- and C-terminal fragments (N-CaD and C-CaD) were expressed separately in hippocampal neurons. N-CaD enhanced axon extension like full-length CaD, but C-CaD did not (Fig. 3, *B–D*), suggesting that CaD interaction with myosin, but not F-actin, is necessary for CaD-induced axon extension. On the other hand, C-CaD, but not N-CaD, induced formation of the filopodia-like protrusions like full-

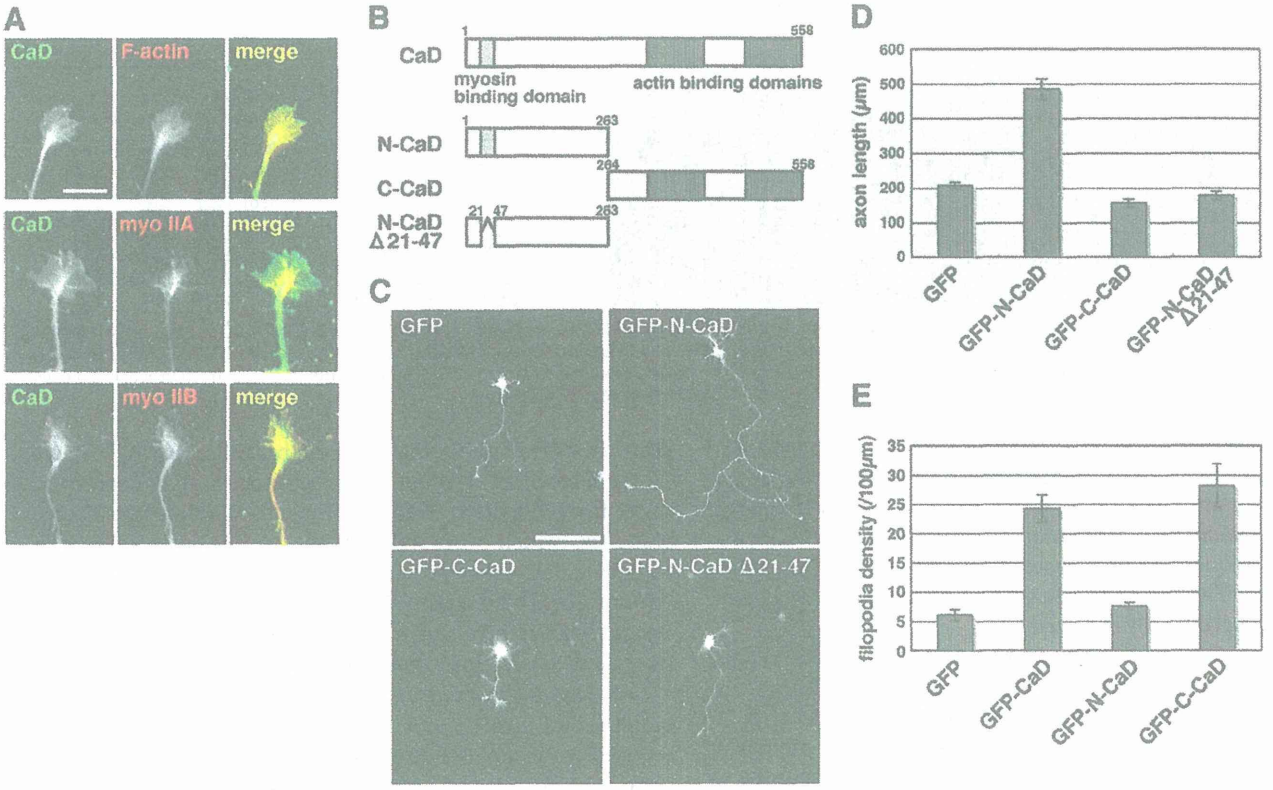

FIGURE 3. **The effect of CaD N- and C-terminal fragments on axon extension.** *A*, CaD, myosin IIA, and myosin IIB localization in the hippocampal neuron axonal growth cone. Bar, 10 μm. *B*, CaD domain structure. *C*, morphology of neurons cultured for 3 days after transfection with GFP, GFP-N-CaD, GFP-C-CaD, or GFP-N-CaD Δ21–47 (bar, 100 μm.), and *D*, quantification of their axonal length. Data are means ± S.E. of values from four to six independent experiments. *E*, quantification of their filipodial density. Data are means ± S.E. of values from four to six independent experiments.

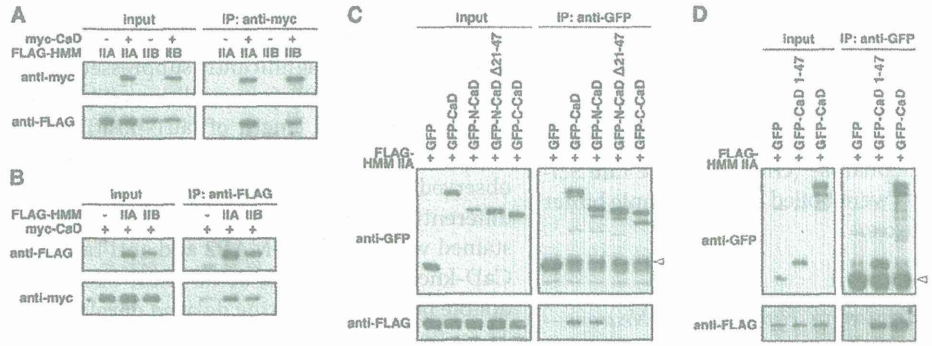

FIGURE 4. **CaD and myosin II interactions.** *A*, HEK 293T cells transfected with myc-CaD and FLAG-HMM IIA or FLAG-HMM IIB were immunoprecipitated using anti-Myc antibody or *B*, anti-FLAG antibody. *C*, HEK 293T cells were transfected with FLAG-HMM IIA and GFP, GFP-CaD, GFP-N-CaD, GFP-N-CaD Δ21–47, or GFP-C-CaD and immunoprecipitated with anti-GFP antibody. *Arrowhead*: IgG light chain position. *D*, HEK 293T cells were transfected with FLAG-HMM IIA and GFP, GFP-CaD Δ21–47, or GFP-CaD and immunoprecipitated with anti-GFP antibody. *Arrowhead*: IgG light chain position.

length CaD (Figs. 1*F* and 3, *C* and *E*), suggesting that this effect is dependent on the C-terminal actin binding domains.

Co-immunoprecipitation was used to determine whether non-muscle myosin II, like smooth- and skeletal-muscle myosins, binds to CaD. Because CaD is reported to bind to the S-1 and S-2 regions of smooth and skeletal muscle myosins (23), we examined CaD interactions with myosin IIA or IIB N-terminal fragments, which are composed of a globular head domain, a neck region, and a small tail fragment corresponding to heavy meromyosin (HMM). As with smooth and skeletal muscle myosins, CaD bound to HMM IIA and IIB, and CaD's C-terminal F-actin-binding domains were not necessary for these interactions (Fig. 4, *A–C*).

Previous studies demonstrated that the 27-amino acid sequence in CaD's N terminus (Tyr-21 to Lys-47 in human l-CaD) is necessary for binding to smooth-muscle myosin (24). N-CaD Δ21–47 fragment, in which this 27-amino acid sequence is deleted, did not interact with HMM IIA, and a CaD fragment including amino acids 1–47 was the minimum required for HMM IIA binding (Fig. 4, *C* and *D*). Importantly, N-CaD Δ21–47 fragment completely lost the ability to enhance axon extension (Fig. 3, *C* and *D*), strongly supporting the idea that CaD is accumulated in the growth cone as

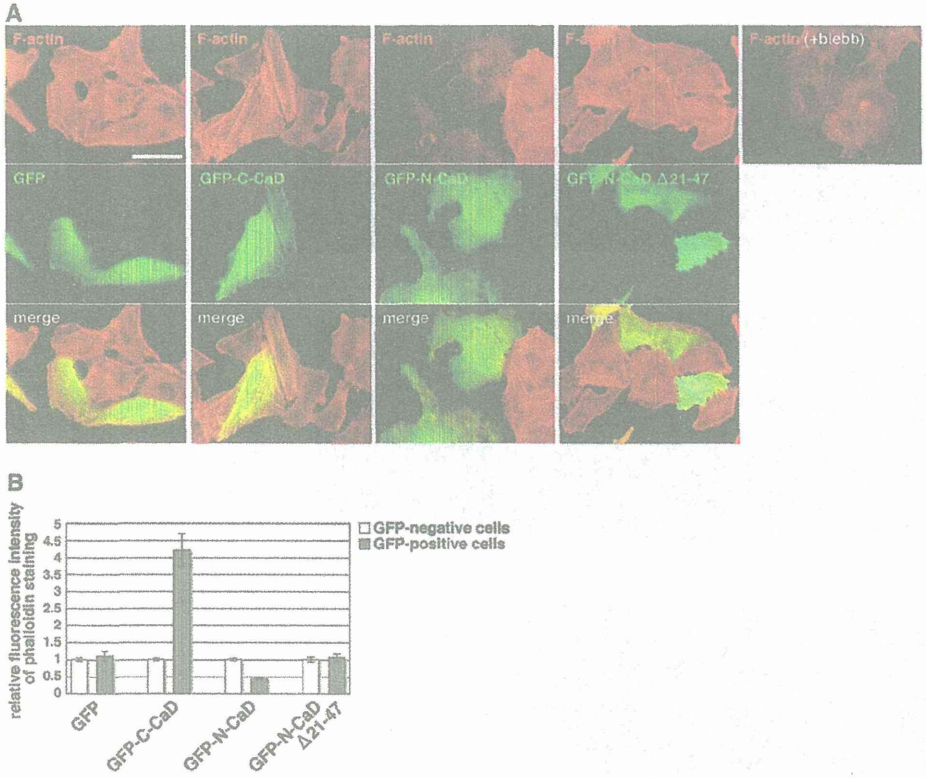

FIGURE 5. **CaD fragments ectopically expressed in A549 cells.** A549 cells transfected with GFP, GFP-C-CaD, GFP-N-CaD, or GFP-N-CaD Δ21–47 were fixed and stained with anti-GFP antibody (*green*) and phalloidin (F-actin, *red*). At right, cells were treated with 10 μM blebbistatin (blebb) for 30 min and then fixed and stained with phalloidin. Bar, 100 μm. *B*, quantification of fluorescence intensity of phalloidin staining in GFP-positive and GFP-negative cells, respectively.

an actomyosin component and enhances axon extension through direct interaction with non-muscle myosin II.

N-CaD Exhibits the Same Effect as Blebbistatin—To determine the significance of CaD interaction with myosin, N-CaD or C-CaD was transfected into A549 cells. CaD has been reported to stabilize actin filaments via its C-terminal F-actin-binding domains, causing thick actin fibers to form (12, 26). In A549 cells, C-CaD strongly induced thick actin fiber formation (Fig. 5, *A* and *B*). On the other hand, cells expressing N-CaD showed significant actin fiber loss and a flat cell shape with prominent lamellipodia (Fig. 5, *A* and *B*). These effects were completely lost in A549 cells expressing an N-CaD Δ21–47 fragment lacking the 27-amino acid myosin-binding sequence (Fig. 5, *A* and *B*). Further, these morphological changes were very similar to those found in cells treated with the myosin II-inhibitor blebbistatin (Fig. 5*A*). These results suggest that CaD binds to myosin at its N terminus, and that it inhibits myosin II function independently of its C-terminal F-actin-binding domains.

CaD Changes Growth Cone Morphology and Myosin II Localization—To determine the function of CaD in growth cones, we observed growth cone morphology and myosin II localization in the hippocampal neurons expressing CaD fragments (Fig. 6). N-CaD inhibited lamellipodia expansion, whereas C-CaD enhanced filopodia formation in growth cones. Full-length CaD induced both lamellipodia retraction and filopodia formation. N-CaD Δ21–47 had no effect on growth cone morphology.

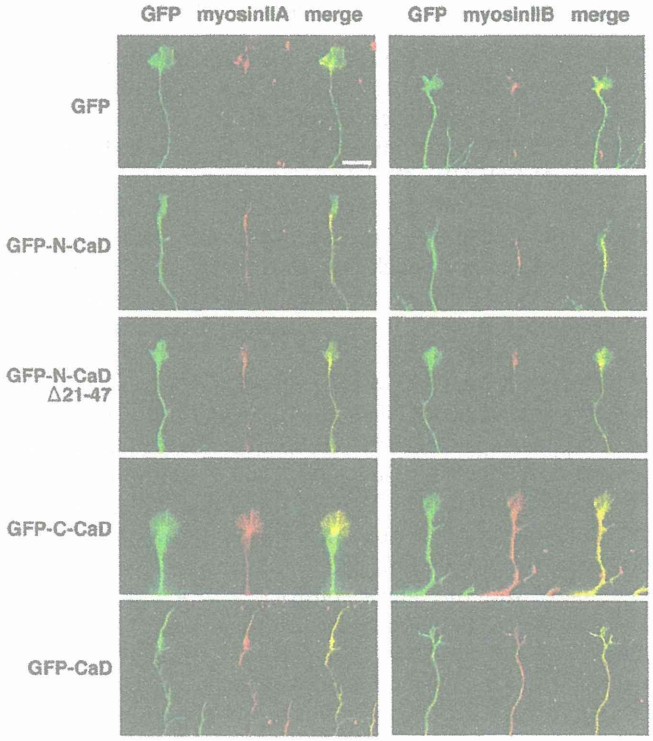

FIGURE 6. **The effect of CaD fragments on growth cone morphology and myosin II localization.** Hippocampal neurons transfected with GFP, GFP-C-CaD, GFP-N-CaD, GFP-N-CaD Δ21–47, or GFP-CaD were fixed and stained with anti-GFP (*green*) and anti-myosin IIA or IIB (*red*) antibodies. Bar, 10 μm.

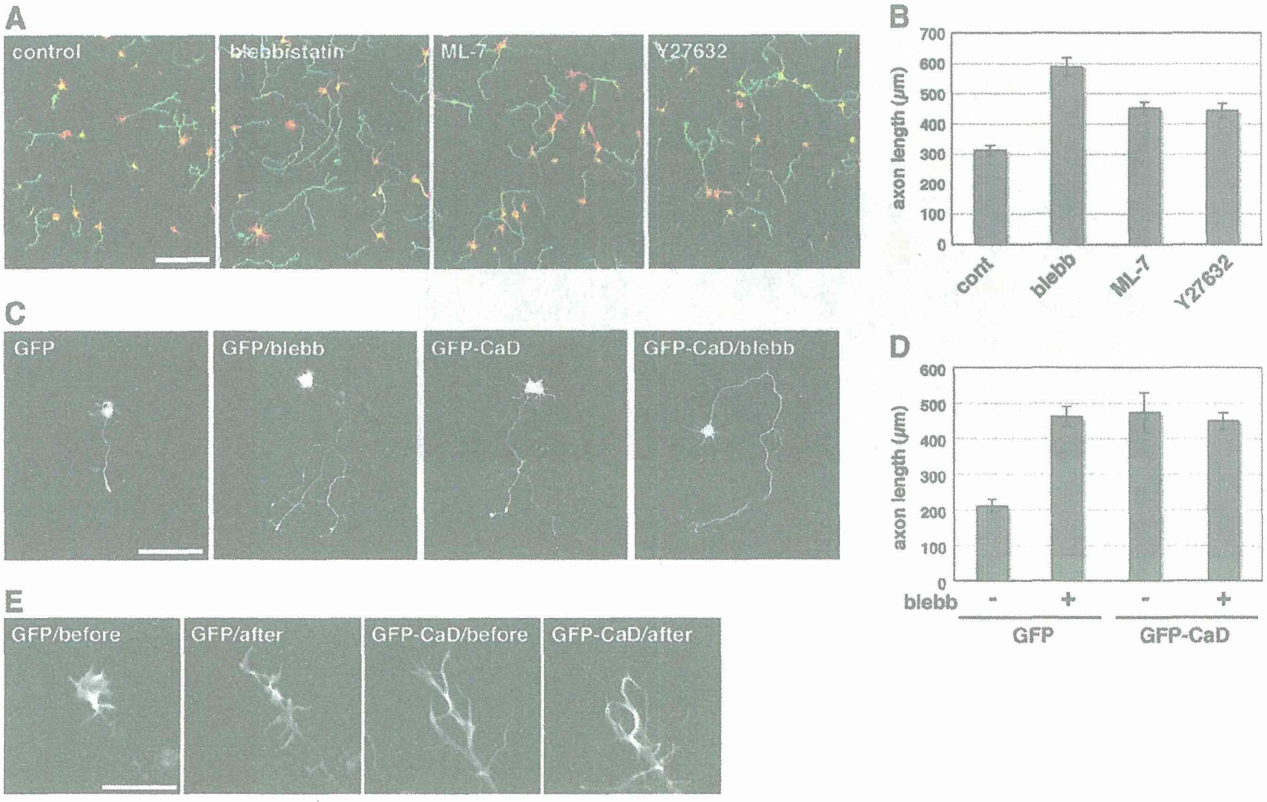

FIGURE 7. **Myosin II functions in CaD-enhanced axon extension.** *A*, hippocampal neurons were cultured with 10 μM blebbistatin, 50 μM ML-7, or 10 μM Y27632 for 3 days, and then fixed and stained with anti-tau1 (*green*) and anti-MAP2 (*red*) antibodies (bar, 400 μm.); *B*, quantification of axonal length in these neurons. Data are means ± S.E. of values from at least 70 cells. *C*, primary cultured hippocampal neurons transfected with GFP or GFP-CaD and incubated with or without 10 μM blebbistatin for 3 days (bar, 100 μm); *D*, quantification of axonal length in these neurons. Data are means ± S.E. from four independent experiments. *E*, growth cone morphology in GFP- or GFP-CaD-transfected neurons before or after treatment with 10 μM blebbistatin for 30 min. To visualize F-actin in living neurons, the cells were transfected with mcherry-LifeAct. Bar, 20 μm.

In GFP-N-CaD-transfected neurons, myosin II staining was slightly diffuse, but distinctly strong in the basal region of the lamellipodia-poor growth cones. In the cells transfected with GFP-CaD and GFP-C-CaD, myosin II was tightly associated with filopodia. N-CaD Δ21–47 had no effect on myosin II localization. These results indicate that C-terminal actin binding domains enhances actin bundling in growth cones, leading to filopodia formation, with which myosin II associates. On the other hand, N-terminal myosin-binding domain inhibits lamellipodia formation in growth cone, but scarcely have an effect on the myosin II localization.

CaD Enhances Axon Extension by Inhibiting Myosin—To examine how inhibiting myosin function would affect axon extension, hippocampal neurons were incubated with blebbistatin, myosin light chain kinase inhibitor ML-7, or Rho-associated protein kinase inhibitor Y27632, drugs that directly or indirectly inhibit myosin function. All of these drugs, especially the direct inhibitor blebbistatin, significantly increased axonal length compared with the vehicle control (Fig. 7, *A* and *B*). In GFP-CaD-transfected hippocampal neurons, however, blebbistatin did not further accelerate axon extension (Fig. 7, *C* and *D*). Coupled with its effects on axon extension, blebbistatin induced morphological changes in the axonal growth cones, inducing a switch from lamellipodial to filopodia-like protrusions (Fig. 7*E*). In the GFP-CaD-transfected neurons, axonal growth cones displayed a filopodia-like morphology without expanded lamellipodia, and their morphology was not affected by blebbistatin treatment (Fig. 7*E*). These findings indicate that blebbistatin and CaD enhance axon extension via the same pathway, through which myosin II function is inhibited.

DISCUSSION

CaD is a ubiquitous regulator of the actin cytoskeleton. Most of CaD functional domains that bind F-actin, tropomyosin, and calmodulin are located in its C terminus, and the C-terminal fragment can inhibit myosin ATPase activity and stabilize actin filaments (8, 12, 26–28). CaD N-terminal region also has a myosin-binding sequence, through which CaD binds to smooth and skeletal muscle heavy meromyosins (23). This binding domain is probably involved in tethering myosin to actin filaments (22, 29), but the significance of myosin binding to CaD had been unclear. In our present study, we clearly demonstrated that CaD enhances axon extension through direct interaction with non-muscle myosin II via its N-terminal myosin-binding sequence. N-CaD, which lacks the all C-terminal functional domains, exhibited the same effect on axon extension as full-length CaD (Fig. 3, *C* and *D*), indicating that axon extension does not depend on the CaD-mediated physical bridge between myosin and actin.

In addition to axon extension, CaD induced formation of the filopodia-like protrusions from soma and axon branches (Figs. 1*F* and 3*E*). CaD also enhanced filopodia formation in growth